

1 First Results of Mars Express - ExoMars Trace Gas Orbiter Mutual 2 Radio Occultation

3 Jacob Parrott¹, Håkan Svedhem², Olivier Witasse³, Colin Wilson³, Ingo Müller-Wodarg¹,
4 Alejandro Cardesín-Moinelo^{4,5,6}, Peter Schmitz⁷, James Godfrey⁷, Olivier Reboud⁷, Bernhard
5 Geiger⁴, Beatriz Sánchez-Cano⁸, Bruno Nava⁹, and Yenca Migoya-Orué⁹

6 ¹Imperial College London, London, UK

7 ²TU Delft, Delft, The Netherlands

8 ³European Space Research and Technology Centre, ESA-ESTEC, Noordwijk, The Netherlands

9 ⁴European Space and Astronomy Centre, ESA-ESAC, Madrid, Spain

10 ⁵Instituto de Astrofísica de Andalucía, IAA-CSIC, Granada, Spain

11 ⁶Instituto de Astrofísica e Ciências do Espaço, IA, Lisbon, Portugal

12 ⁷European Space Operations Centre, ESA-ESOC, Darmstadt, Germany

13 ⁸School of Physics and Astronomy, University of Leicester, Leicester, UK

14 ⁹STI Unit, The Abdus Salam International Centre for Theoretical Physics, Trieste, Italy

15 May 21, 2024

16 Abstract

17 Spacecraft-to-spacecraft radio occultations experiments are being conducted at Mars between Mars Express
18 (MEX) and Trace Gas Orbiter (TGO), the first ever extensive inter-spacecraft occultations at a planet other than
19 Earth. Here we present results from the first 83 such occultations, conducted between 2nd Nov 2020 and 5th of
20 July 2023. Of these, 44 observations have to-date resulted in the extraction of vertical electron density profiles.
21 These observations are the successful results of a major feasibility study conducted by the European Space Agency
22 to use pre-existing relay communication equipment for radio science purposes. Mutual radio occultations have
23 numerous advantages over traditional spacecraft-to-ground station occultations. In this work, we demonstrate
24 how raw data are transformed into electron density values and validated with models and other instruments.

25 1 Introduction

26 A radio occultation (RO) observation occurs when a radio transmitter and the receiver become occluded from each
27 other by an atmosphere. Just before the signal is lost, the vector between the two antennae carves through the
28 planetary limb, going successively deeper until it reaches the surface. As the vector passes through atmospheric
29 mediums of different refractive properties, the signal is imparted with a small frequency shift. These refractive
30 properties can be inferred after the measurement has taken place by looking for the frequency shift that remains
31 after the Doppler shift due to the relative motion of the two spacecraft has been factored out. In turn, these
32 refractive properties can be used to estimate the density of the neutral atmosphere and the electron density of
33 the ionosphere. Conventionally, RO for other planets apart from Earth happens between a spacecraft orbiting said
34 planet and a ground station on the Earth's surface. However this can also occur between two spacecraft orbiting
35 the same planet, which is called Mutual Radio Occultation (also known as Crosslink Occultation), and is the topic
36 of this study.

37
38 Mutual RO for planets other than Earth is relatively new, having only three previous trials during 2007 between
39 Mars Reconnaissance Orbiter and Mars Odyssey (Ao et al., 2015). Since then it has not been revisited, despite its
40 numerous benefits over conventional spacecraft-to-earth RO. Benefits include improved spatial distribution across
41 a range of latitudes, a better range of Solar Zenith Angles (SZA), a higher Signal-to-Noise (SNR) because the
42 transmitter and receiver are far closer and finally, simpler processing because the Earth's atmospheric parameters
43 do not need to be accounted for in the data reduction.

44
45 This paper describes the spacecraft configuration in Section 3. As a large component of this feasibility study was
46 choreographing the two spacecraft, emphasis will be given to the planning stages and the antenna setup. The
47 information on how to obtain electron density profiles from the raw data obtained at TGO is provided in Section
48 4. This is followed by presenting examples of two representative electron density profiles in Section 5. We finish

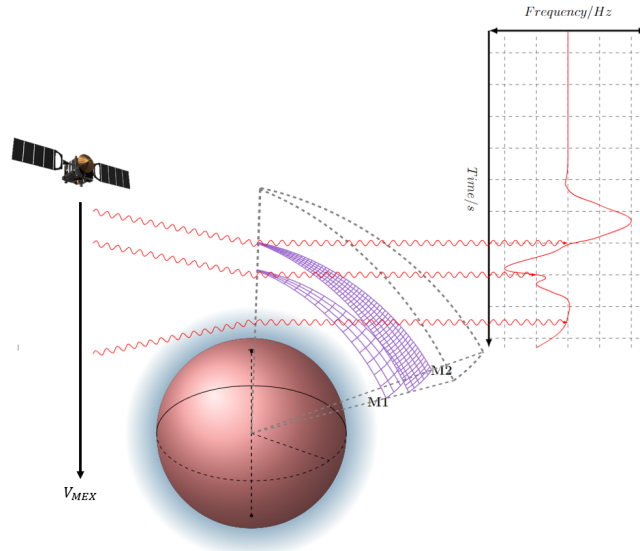


Figure 1: Schematic of Mutual RO in the Martian environment (not to scale). On the left is a transmitting spacecraft moving downwards in an ingress configuration. The red lines represent radio waves being transmitted from the transmitter. The receiving satellite has been omitted for clarity. As the tangent point descends, the radio link first passes through the ionospheric layers (shown as M1 and M2), and later also passes through the neutral atmosphere (shown in a blue shade). The direction of the transmitted waves bend according to the mediums refractivity, such that the $n < 1$ ionosphere bends the waves away from the planet, and the $n > 1$ neutral atmosphere refract the waves towards the planet. A frequency shift is imparted onto the radio link due to the refraction in the Martian ionosphere and atmosphere. The red radio wave lines can be used for mapping the specific features in the Martian ionosphere and atmosphere to the features in the vertical frequency plot.

49 with a discussion in Section 6, this section will breakdown the rationale for certain engineering decisions. As this
 50 work is concentrated on the engineering of mutual RO, the scientific analyses and discussions of the shape of the
 51 profiles, such as ionosphere structure and formation, are outside the scope of this article and will be addressed in
 52 a separate study.

53 2 Orbit Configuration for Mutual Radio Occultation

54 In our experiment, the two satellites that are being used are the European Space Agency’s (ESA) Mars Express
 55 (MEX) and ExoMars Trace Gas Orbiter (TGO).

56
 57 There are several advantages to the mutual configuration over the ‘conventional’ spacecraft-to-Earth occultations.
 58 For instance, the latitudes of conventional occultation measurements are similar between successive orbits. Over
 59 a matter of weeks, conventional occultation events vary in Martian latitude by less than 10° . This means that in
 60 a particular Martian season, only a limited range of latitudes can be measured (e.g. only Polar or only equatorial
 61 regions.) This is due to the heliocentric layout of Mars and Earth being similar from day-to-day and the fact that
 62 the nodal procession of the spacecrafts’ orbit is slow; therefore, the Mars-Earth horizon occurs in a similar posi-
 63 tion. Figure 3 highlights this, by showing that TGO-Earth and MEX-Earth conventional occultations are restricted
 64 to very specific latitudes for a short timescale, whereas the orbits of MEX and TGO (shown in Table 1) produce a
 65 far broader latitudinal coverage. Also, spacecraft-to-Earth occultations can only occur in specific seasons along the
 66 martian year, whereas mutual RO occur more regularly.

67
 68 Similarly, due to the relative positions of Mars, Earth and the Sun, the spacecraft-to-Earth RO is also constrained
 69 to similar values of local time and SZA in any given season. A rough guide for the possible range of SZA for
 70 occultations with Earth has been provided by Tamburo et al., 2023, with $90 \pm 180 \times 1AU/\pi a$, where a is the
 71 semi-major axis of the orbit of the occulted planet, in astronomical units. This simple formula loosely applies to
 72 Mars occultations as it does not account for the relatively larger eccentricity of the Martian orbit. For example, in
 73 a three month period, TGO-Earth RO only covers SZA of 81° - 130° (ingress) and 50° - 100° (egress), while mutual
 74 occultations offer a much more even distribution of SZA, as shown in Figure 4.

75
 76 A further advantage of mutual ROs is that of signal quality. Having the receiver and transmitter orbiting the same

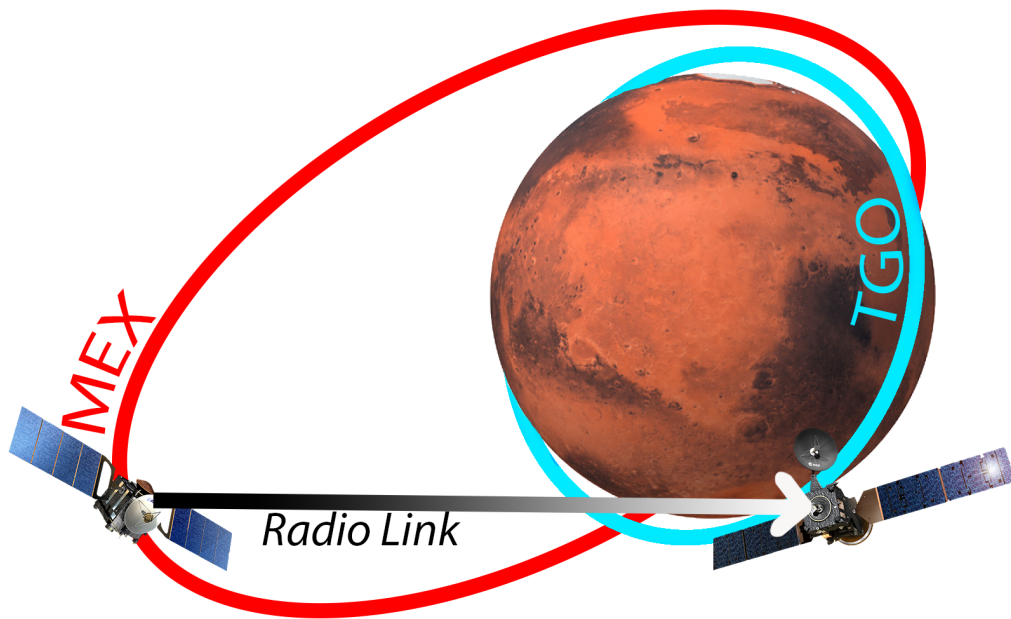


Figure 2: Orbital Configuration of MEX (red) and TGO (blue) during a typical mutual radio occultation observation, with a black/white arrow indicating the direction of the radio link between the two spacecraft

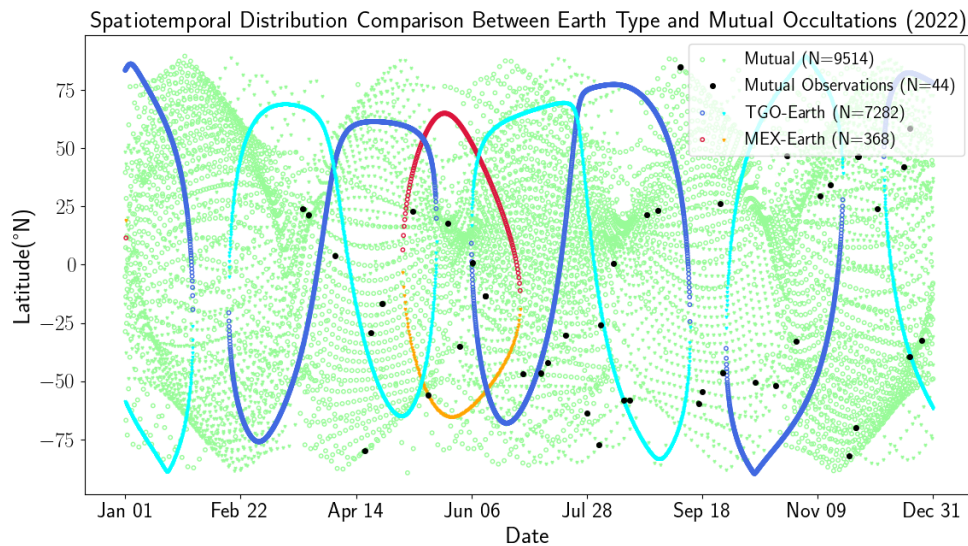


Figure 3: Spatiotemporal distribution of all potential RO opportunities for the year 2022. Shown are TGO-Earth (blue) and MEX-Earth (red) RO having a periodicity through the year and limited coverage. Ingress are indicated by darker colours and Egress occultations have a lighter hue. Mutual RO opportunities (green) are shown to have a considerably more even spaced distribution in latitudes. Actual Mutual RO observations that have been conducted in this study are indicated by solid black circles

Radial Histogram for Solar Zenith Angle of Different Occultation Types (01/05/22 - 01/08/22)

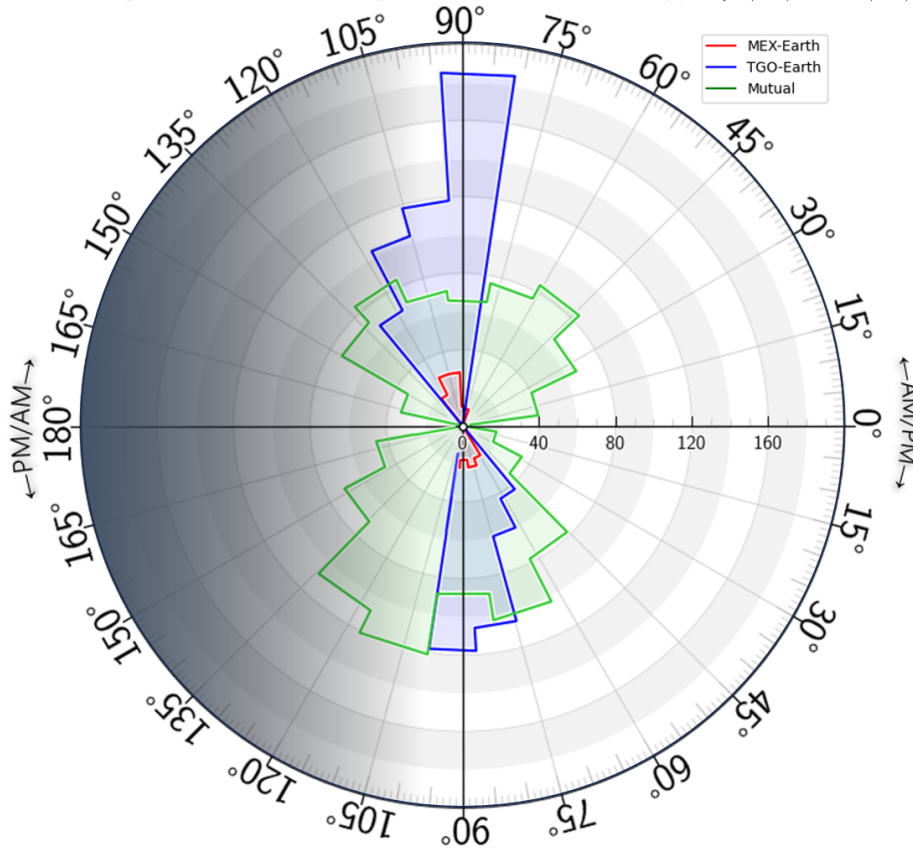


Figure 4: Radial histograms to indicate the Solar Zenith Angle (SZA) distribution of all spacecraft-to-Earth and spacecraft-to-spacecraft (Mutual) (green) RO opportunities during a three month period in 2022. SZA is indicated around the circumference and population is shown on the x-axis within the plot. This plot shows that TGO-Earth (blue) and MEX-Earth (red) RO cluster in a specific SZA dawn/dusk range during this period, whereas the mutual occultations cover most SZA values. The total number of MEX-Earth RO opportunities is smaller than the number of TGO-Earth RO opportunities due to MEX's longer orbital period.

planet means that interplanetary plasma does not have to be accounted for in the data analysis. For spacecraft-to-Earth occultations, the resultant frequency shift can be affected by heliophysical parameters, such as the integrated interplanetary plasma along the signal path instead of the target ionosphere or atmosphere, restricting the range of reliable sounding. Additionally, not having the receiver inside the atmosphere of the Earth and under its significantly denser ionosphere and moist troposphere greatly simplifies the processing of the data since meteorological datasets do not have to be integrated into the processing, hence removing a potential source of error. Finally, mutual ROs are typically performed over a range of 1,000 - 10,000 km. With the aid of orbit simulations, we calculated this to be some five orders of magnitude smaller than the 55 - 400 million km range over which Mars-to-Earth radio occultations are carried out, resulting in a significantly better SNR.

Orbit parameters	Transmitter (MEX)	Receiver (TGO)
Pericentre altitude (km)	350	380
Apocentre altitude (km)	10500	430
Eccentricity	0.57	0.007
Inclination (°)	87	76
Period (hours)	7.5	2

Table 1: Approximate orbit characteristics of the transmitting and receiving satellites. See (Cardesín-Moinelo et al., 2021) and ESA SPICE kernels (European Space Agency & ESA SPICE Service, 2019a) (European Space Agency & ESA SPICE Service, 2019b) for detailed orbital parameters

The orbits of the two spacecraft also dictate whether a mutual RO will be considered an ingress or an egress observation. This is decided on whether the tangent point goes up or down in altitude during the measurement. The tangent point refers to the 3D location in the vector between the two spacecraft (SC) that is closest to the planet's surface. The tangent point during an RO observation can either be increasing or decreasing in altitude. This is because Mutual RO has two configurations: as previously described, the two satellites can begin the observation in-view of each other, then they can descend over the horizon with respect to each other. For the example in Figure 1, we call this an ingress RO because the tangent point moves monotonically downwards. But mutual RO can also work in reverse, where the measurements begins when the receiving satellite is occluded by the surface of a planet. As the RO observation progresses, the tangent point increases in altitude and the observation ends when this tangent point is far above the ionosphere; this is known as egress RO.

3 Experiment configuration and operations

TGO is the orbital element of the ExoMars programme. TGO and the Schiaparelli Entry, Descent and Landing Demonstrator Module (EDM) were launched together on March 14th, 2016 and arrived at Mars seven months later (Ball et al., 2022). TGO carries four advanced scientific instruments and is also serving as a member of the Mars Relay Network. At present, while waiting for the arrival of the ESA Rosalind Franklin rover, TGO relays over 50% of the data from the NASA Landers back to Earth.

ESA's first mission to another planet, Mars Express (MEX), was launched on June 2nd, 2003 arriving at Mars on December 25th of the same year. Its Beagle-2 lander was declared lost in February 2004 after repeated attempts to contact the lander failed (Cardesin-Moinelo et al., 2024) (Bridges et al., 2017). The UHF radio included on MEX to act as the lander relay for Beagle-2 subsequently has performed relay operations with 6 NASA landers: Spirit, Opportunity, Phoenix, Curiosity, InSight and Perseverance as well as the Chinese Zhurong rover, in addition to tracking the ExoMars Schiaparelli demonstrator during its descent through the Martian atmosphere in 2016.

3.1 MEX transmitter - MELACOM

MELACOM (Mars Express LAnder COMmunication) was chosen to be the transmission source as its Open Loop recording capability is much less than that of TGO's Electra unit and wouldn't be able to record a signal with sufficient precision and sampling rate for radio science observations (James Godfrey, 2020, *pers comm*). However, MELACOM's oven stabilised oscillator means that it could potentially provide a stable carrier signal. The oscillator's Allan variance is stated to be better than 5×10^{-12} (C-MAC, 2005), which is considered to be very good, even if it is not as good as an Ultra Stable Oscillator (USO).

In normal lander data relay use, the MELACOM radio transmits a hail signal at the target lander. On receiving

119 the hail, the lander responds and following a handshake the radio link between the two spacecraft is established.
 120 From that point onwards, data can be transferred between the two spacecraft in either direction. The hail sequence
 121 comprises of brief periods of unmodulated carrier transmission, followed by a modulated signal and then a drop
 122 in transmission repeating every 22 seconds. This is not suitable for the radio science experiment. It was, however,
 123 used for the first eight 'proof of concept' measurements. The manufacturer of the MELACOM radio, QinetiQ UK,
 124 produced an updated version of the MELACOM firmware including a new unmodulated 'carrier-only' transmission
 125 mode. After testing this firmware on the avionic test bench, this firmware update was up-linked and tested in-flight
 126 in March 2021 and has been used for all subsequent observations.
 127 In preparation for the ExoMars arrival at Mars, a performance characterisation of the MELACOM system, including
 128 the oscillator accuracy, was done from the Arecibo radio telescope in November 2013. It was determined that the
 129 frequency only differed from the nominal frequency by 52 Hz (Gurvits, 2014). This is well in line with the expected
 130 ageing since the launch.

131 3.2 TGO receiver - Electra

132 Electra is a modern highly flexible UHF communications system designed by NASA's Jet Propulsion Laboratory
 133 (JPL)(Edwards, 2003) and is presently flying on several NASA missions. It was provided by NASA to ESA as a part
 134 of the ExoMars collaboration. It can operate at 16 different transmit frequencies and 16 receive frequencies in any
 135 combination in the 390-450 MHz band (Taylor et al., 2006). For these MEX-TGO RO measurements, the receiving
 136 frequency was set to the nominal MEX transmission frequency of 437.1 MHz. The recording is done in Open Loop
 137 Recording mode, i.e., there is no attempt to lock on the incoming signal and the recorder is running 'in the blind'
 138 at a sampling frequency up to 128 kHz. Both In-phase and Quadrature signals are sampled simultaneously. This
 139 sample frequency is more than sufficient to account for the worst case expected frequency shift, so to ensure that
 140 the signal always is within the bandwidth of the system. At a later stage it may be decided to lower the sampling
 141 rate to reduce the generated data volume.

142 On Mars Reconnaissance Orbiter (MRO), Electra is driven by Ultra Stable Oscillators (USO) providing excellent
 143 short and long term frequency stability to the units. Unfortunately, this is not the case for Electra on TGO where
 144 a Temperature Compensated Crystal Oscillator (TCXO) is used. It is adequate for the purpose of communication
 145 with the units on the Martian surface but is marginal when used for Radio Science. At present, however, it has
 146 not been possible to quantify in detail how the performance of the RO is affected by the TCXO and its ageing.
 147 A difference between measurements and predictions in the absolute frequency of several hundred Hz has been
 148 observed. This has been identified as a spread in the exact frequencies from the various different units that had
 149 not been accounted for in a parameter table. This has now been corrected by updating a time conversion constant
 150 within Electra but there is a remaining difference of about 120 Hz. This may be due to ageing of the crystal in the
 151 oscillator and is not a major problem as it can easily be subtracted.

152 3.3 The MEX-TGO Radio Link

153 The receiving frequency of one of the two spacecraft had to be changed to match the transmit frequency of the
 154 other since the Orbiter-to-Lander UHF communication radios are used here for a direct link between the two
 155 orbiters, meaning one SC must either transmit at a receiving frequency or receive at a transmit frequency. Fortu-
 156 nately, the TGO Electra radio can accomplish this, whereas the MEX MELACOM radio lacks this versatility. TGO
 157 was therefore configured to receive at 437.1 MHz, the transmit frequency of the MEX relay radio.

158
 159 Conventional ROs usually utilise the spacecraft's deep space communication equipment, typically at X-band and/or
 160 S-band (8-12 GHz and 2-4 GHz, respectively) (Withers et al., 2020)(Pätzold et al., 2004). Here we describe our
 161 experimental work using the ultra high frequency (UHF) radio packages onboard MEX and TGO (390-450 MHz),
 162 originally designed for communication with landers and rovers on the Martian surface.

163
 164 RO at UHF frequencies are especially effective for measuring ionospheres. This is due to the specific plasma fre-
 165 quency of the ionosphere, which occurs when electron and ion momentum acts as a restoring force against an
 166 electric field between an electron and an ion. This frequency increases with electron density such that,
 167

$$f_p = \frac{1}{2\pi} \sqrt{\frac{N_e e^2}{m \xi_0}} \quad (1)$$

168 where N_e is the electron density, e is the elementary charge, m is the electron mass and ξ_0 is the permittivity of free
 169 space. For frequencies below the plasma frequency, an incident wave will be fully reflected. For frequencies much
 170 higher than the plasma frequency, an incident wave will propagate with only little effect through the medium.

Parameters	Values
Tx	
RF Power	37 dBm (5W)
Antenna Gain	-7 dBi
Circuit Loss	-1 dB
Transmitted Power	29 dBm
Medium	
Space Loss	-168.1 dB
Boresight Compensation	6 dB
Rx	
Antenna Gain	-7.1 dBi
Circuit Loss	-0.4 dB
Error Propagation	
Total Received Power	-140.6 dBm
Noise Spectral Density	-171.6 dBmHz ⁻¹
Rx Power / Noise (1 second)	31 dBHz
Carrier Loop Bandwidth	1 Hz
Radio Loss	-1 dB
Carrier Loop SNR	30 dB
Voltage SNR (1 second)	44.8
Phase Error	22.3 mrad
Pathlength Error	2.4 mm
Frequency Error	3.6 mHz

Table 2: The worst case link budget and physical error propagation for a MEX-TGO Mutual RO observation with the maximum distance and off-boresight angles

171 However, for frequencies only slightly above the plasma frequency, an incident wave will propagate through the
 172 medium but will be refracted and will experience a phase shift. We make use of this effect for RO measurements.

173 With $n^2 = 1 - \frac{\omega_p^2}{\omega^2}$, where $\omega_p = 2\pi f_p$, ω is the transmit radio frequency and n is the refractive index (Born & Wolf,
 174 2019), it can be seen that the lower the frequency is, the higher the effect will be on the propagation, as long as
 175 the frequency is above the plasma frequency. Therefore, at UHF the effect is much stronger than it is at S- or X-
 176 band.

177 Apart from the frequency selection, the specifics of the radio link should be discussed. The maximum distance
 178 between the two spacecraft during an RO can be up to approximately 15,000 km. In order not to interfere with
 179 scientific observations by any of the other investigations on MEX or TGO, no dedicated pointing is used for the
 180 RO sessions. Both S/C are usually pointing with the sides carrying their UHF antennas to near Nadir. There-
 181 fore, the off-bore-sight angles towards each other are typically below 75°. Maximum distance and maximum off
 182 bore-sight pointing on both S/C never occur simultaneously because MEX's MELACOM antenna is always near
 183 nadir at apoapsis, therefore pointing towards the lower altitude TGO. Therefore, a compensation of +6 dB has
 184 been applied to this worst case scenario. The minimum expected received power at Electra should be close to
 185 -140.6 dBm at these view angles and ranges, as shown by Table 2. At the UHF frequency (f_t) of 437.1 MHz and
 186 an estimated noise temperature of 500 K, combined with the carrier loop SNR (SNR_{CL}) of 30 dB, would result in
 187 a voltage SNR of 44.8 ($SNR_V = \sqrt{2 \times SNR_{CL}}$). This results in a carrier phase error of just 22.3 mrad (SNR_V^{-1})
 188 leading to a relative pathlength measurement error of 2.4 mm ($SNR_V^{-1}/f_t 2\pi$). Alternatively this is 3.6 mHz error
 189 in frequency. ($(f_t 2\pi - SNR_V^{-1})/2\pi$) So, we anticipate that the contribution of thermal noise will be insignificant
 190 in comparison with systematic errors, for example, oscillator drift.

191

192 3.4 Planning

193 Mutual Radio Occultation uses orbiter communications equipment which is transmitting the same frequency as
 194 used for Orbiter to Lander Forward Link operations. Considering that there are currently 5 Mars orbiters (TGO,
 195 MEX, Mars Reconnaissance Orbiter, Mars Odyssey, and MAVEN) which are communicating in this frequency band
 196 with Mars surface assets, extreme care needs to be given to avoid radio frequency interference (RFI) with other
 197 orbiter to lander relay communications when planning the UHF radio science measurements.

The planning of mutual observations is performed by the Science Operations Centres (SOC) of both MEX and TGO missions (Cardesín-Moinelo et al., 2021). This planning process starts with an opportunity analysis of the geometric conditions, identifying the time periods where the line of sight between MEX and TGO intersects the limb of Mars, when the tangent point altitude is between 0 and 400 km. Also the orientation of both orbiters must be such that the UHF antennas are in view to each other, i.e., both antenna boresight angles are below 75° and the distance between the S/Cs must be less than 15,000 km to ensure a favourable SNR. These visibility windows are then considered potential candidates for Radio Occultation measurements.

The scheduling process then needs to take into account the operational constraints, not only from both spacecraft, but also from any other possible lander relay communications occurring at Mars. Relay operations are considered critical, therefore any orbiter to lander view period is considered as a “no-go zone” for RO observations. These view periods are provided by ESA’s spacecraft operations center (ESOC) to the science operations centers (ESAC), typically 12 weeks prior to the Medium-Term Planning Period which covers 4 weeks of operation. Exclusion periods of special operations by TGO and MEX are also avoided, such as orbit control maneuvers, S/C maintenance periods and MEX communication passes.

Finally, the science planners take all the visibility and feasibility opportunities into account to select the optimal UHF Radio Science observations, either ingress or egress occultations with the best geometrical conditions (lowest distance, best visibility angles, largest altitude range) and maximizing the desired seasonal coverage with respect to latitude, longitude and local time.

Once the UHF Radio Science slots are selected and the full science plan is confirmed for both missions, the science planners at ESAC generate the pointing timeline and the commanding parameters for all MEX and TGO payloads, including the relay antennas, and the timelines are passed on to the mission planners at ESOC for verification, about 8 weeks prior to execution. At this stage the orbiter attitude and spacecraft resource profile (for power consumption and data generation) gets “fixed” and Mission Planners at ESOC provide the selected UHF Radio Science slots to the JPL Mars Relay Operations System (MaROS) as information to the Lander community. This helps to identify potential RFI conflicts in case a relay overflight opportunity comes up at a later stage (e.g. due to updated orbit predictions). In case any RFI conflicts between MEX-TGO Radio Science and NASA relay operations are detected prior to the Short-Term Planning process, when spacecraft commanding is generated, UHF Radio Science observations might have to be withdrawn because relay operations take priority over UHF Radio Science.

Typically, one mutual RO observation is selected every week, covering the limb from the surface up to 400 km, with a default duration of 10 minutes, in which MEX transmits the UHF carrier to TGO, recording in open loop and generating a data volume of about 307 MB. This data is later downlinked to Earth with the same priority as the rest of TGO’s science data and without affecting the relay data traffic.

4 Processing

TGO’s onboard Electra system obtains the downconverted open-loop recordings as in-phase and quadrature data (I&Q). However, the on-ground software package created alongside the system was out-of-date and had not been updated alongside Electra’s firmware upgrades. Therefore, new software was created to read the raw Electra bit-streams to extract the I&Q data, the Automatic Gain Control (AGC) level, and the timestamps.

The following processing chain will be enumerated and its corresponding outputs are found in figure 5.

1. The primary objective for this next processing stage is to extract the peak carrier frequency from the MEX transmission. Firstly, a spectrogram is extracted from the I&Q data by means of a Fast Fourier Transform (FFT) with a 2^{18} point Hanning window, corresponding to 2 s, and an overlap of 50%. With a ten-minute observation and a sampling frequency of 128 kHz, this produces around 585 periodograms. This window size was chosen to get a compromise between frequency resolution and time resolution. The goal was to increase the frequency resolution as much as possible by increasing the window size, to a limit, as a larger window might render the small timescale M1 ionosphere feature indistinguishable. The M1 layer is the fainter secondary ionospheric layer found below the M2 layer. Figure 6 shows two examples of the residual frequency shifts caused by the ionosphere and atmosphere, called the residuum. From the observation on 08/05/23, 450 s marks the M2 features and the smaller bump at 480 s represents the contribution by the M1 ionospheric layer, this is the layer that can be missed if the window size is set too large. For a RO observation with a steep grazing angle, the tangent point is typically within the M1 ionospheric layer for around 10 seconds,

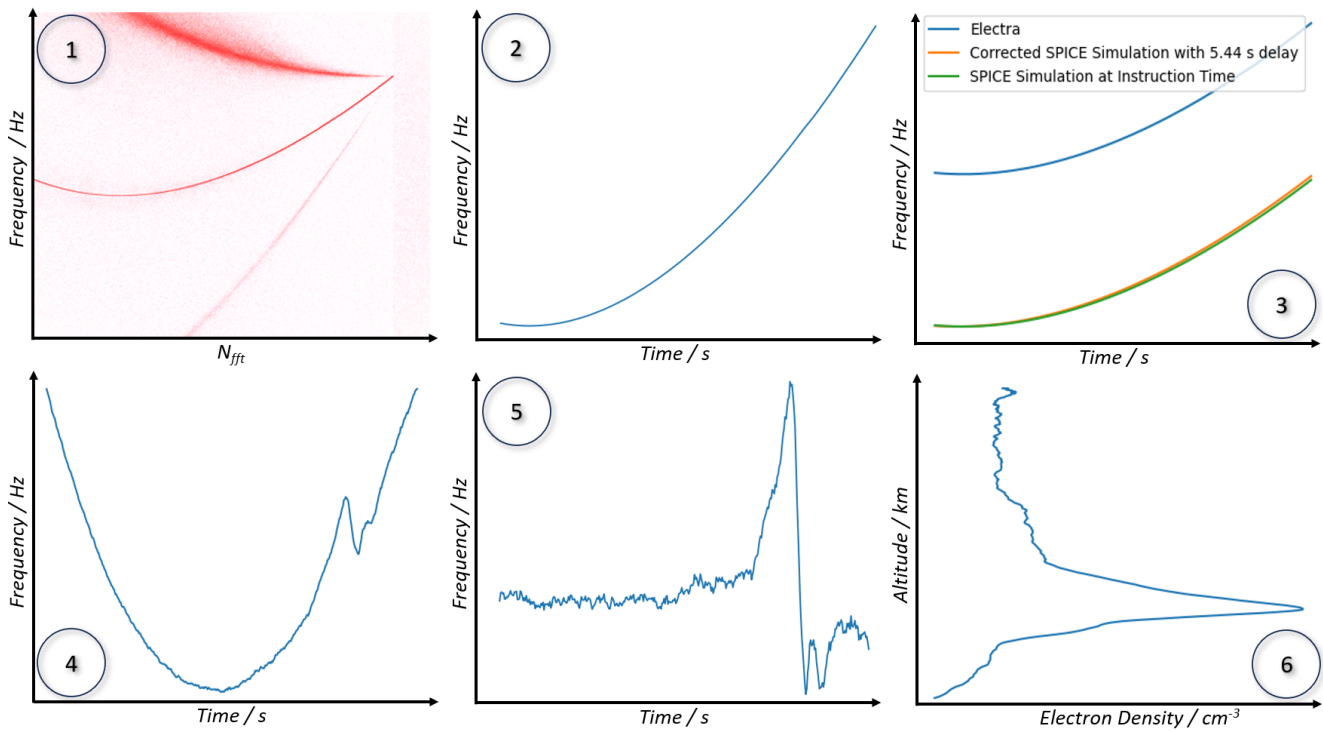


Figure 5: A graphical representation of the outputs to the steps in Section 4. The mechanics of each of these steps are described at length in this section. 1: Spectrogram acquired from performing an FFT on the I&Q data, 2: The carrier in (1) is isolated via selecting the peak spectral densities, then the signal is truncated and has its frequency resolution interpolated, 3: A SPICE Doppler simulation is used to predict what the frequency shift should be if there was just a vacuum between the two spacecraft, 4: The corrected SPICE Doppler signal from (3) is subtracted from the signal (2). Note that the scale is significantly increased in this panel, 5: A low order polynomial fit is removed from (4) and the 70-80 km zero refractivity assumption is leveraged in an Abel-Inversion minimisation. Note that the scale is further increased in this panel, 6: Abel-Inversion and conversion to electron density

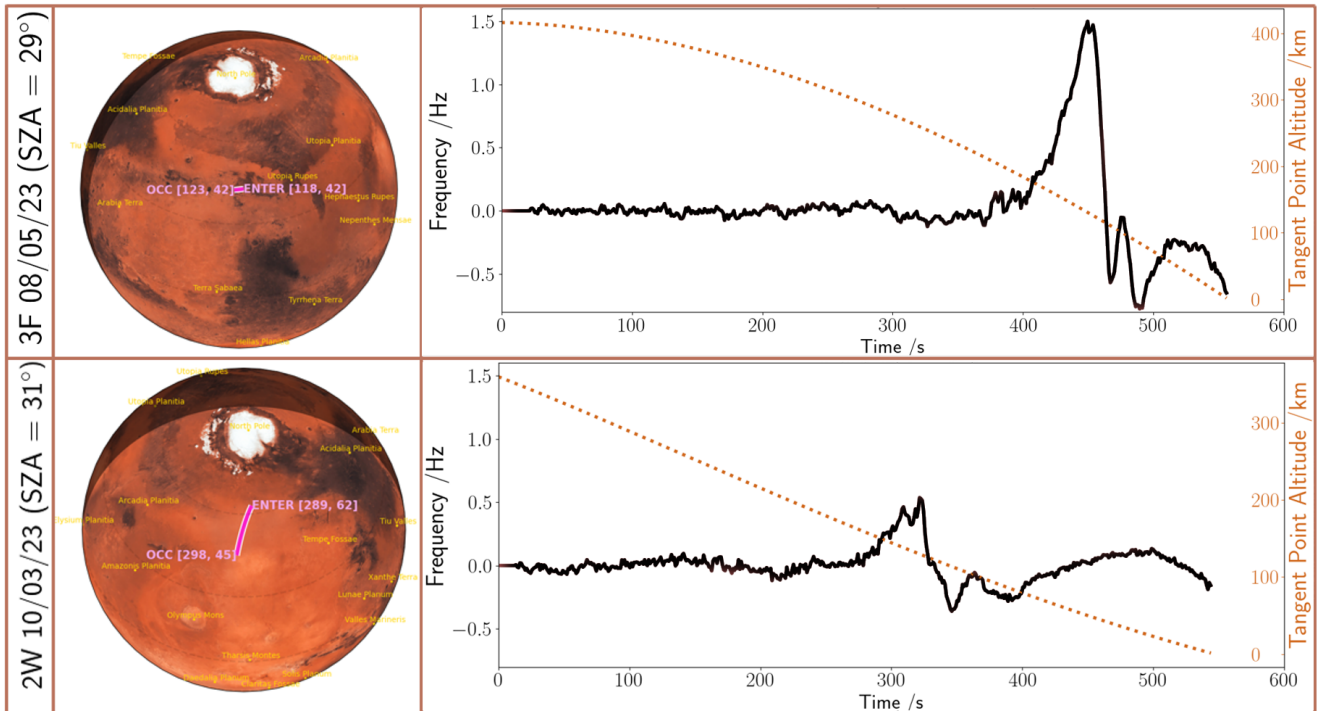


Figure 6: Two residuums to highlight the different features created by the M1 and M2 ionospheric layers, taken from Mutual RO with similar SZA but different grazing angles (the angle between the surface tangent at the point of occultation and the highest altitude tangent point). This shows that the amplitude of the features in the residuum are smaller if the tangent point descends slower, worsening the SNR. This slower descent can be seen by the red dotted line that maps to the right hand side y-axis. On the left is a map of the ground trace (purple line) of the RO, showing the tangent point for the mutual ROs from 08/05/23 and 10/03/23 travelled an arc distance of 219 km and 1051 km, respectively. When future RO opportunities are selected, smaller ground traces are preferred.

254 With current window size, this allows for only nine data points to describe the M1 morphology. Attempting to
 255 increase the spectral resolution anymore by increasing the FFT window size will worsen this.
 256

257 2. Depending on the orbital configuration, the data must then be truncated to exclude times when MEX's tone is
 258 not detected. For ingress occultations, this occurs at the end of the observation as the spacecraft-to-spacecraft
 259 vector is intercepted by the Martian surface, and for egress measurements, this occurs at the beginning and
 260 can be delayed for 10-60 seconds as the MEX-TGO vector is intercepted by the Martian surface. Then, to
 261 increase the frequency resolution further, a Gaussian curve was fitted to the highest spectral density in each
 262 periodogram, these spectral peaks are shown in the two periodograms of Figure 7. The curve fitting was
 263 done on the peak density and its six surrounding points. The mean value in this gaussian (the peak) is taken
 264 as the true received carrier frequency. The lack of resolution would lead to spectral artefacts in the residuum
 265 and ultimately, this reduced the magnitude of these artefacts by 4.8 times.
 266

267 3. The total frequency shift measured by the receiver is dominated by the Doppler shift caused by the relative
 268 velocities of the two spacecraft, hereafter called geometric Doppler. This must be removed from the sig-
 269 nal as it can be three orders of magnitude larger than the frequency shift imparted onto the signal due to
 270 the ionosphere and atmosphere. The geometric Doppler is simulated using SPICE (C. Acton et al., 2018),
 271 an ephemeride framework developed by JPL's Navigation and Ancillary Information Facility (C. H. Acton,
 272 1996). The operational positional kernels for MEX and TGO are updated regularly by the ESA SPICE Ser-
 273 vice, so each simulation uses accurate post-processed spacecraft ephemerides.
 274 Initially, the correct geometric Doppler could not be found as the exact start time for the observation was
 275 not known. As previously mentioned, the timestamps in the bitstream did not reach our required precision,
 276 so the start point for the simulation was based on TGO commanding time, which can vary by ± 16 seconds.
 277 This was overcome by simulating ± 20 geometric Doppler shifts with starting intervals of 1 second and con-
 278 structing a 40 by 600-sized matrix, to which a 2D rectangular bivariate spline was applied. This operation
 279 interpolated the 40 simulations at 10 ms intervals, in effect producing 4000 Doppler shift simulations to
 280 compare against. The geometric Doppler with the smallest difference from frequency recorded at Electra is

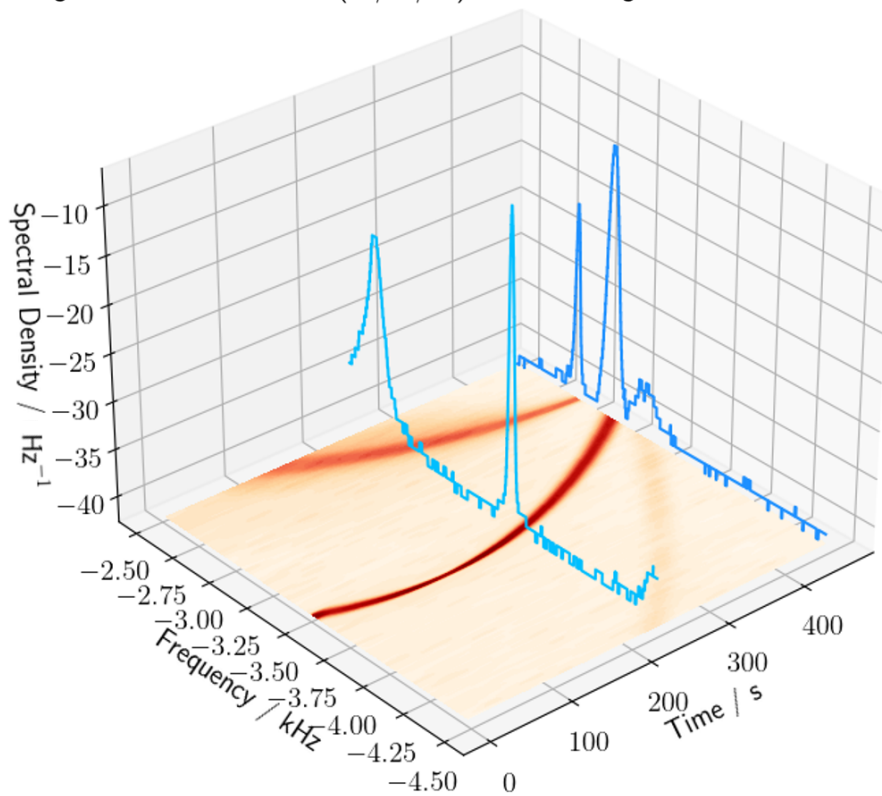
Spectrogram of Electra Dataset (06/04/21) with Periodograms for $N_{FFT} = 240, 440$ 

Figure 7: A spectrogram for an ingress Mutual RO with two periodograms superimposed on the z-axis. The periodograms correspond to the 240th and 440th Fast Fourier Transform (FFT) windows. The darker colours in the spectrogram directly correspond with the larger spectral density seen in the periodograms. As well as showing evidence of multipath scattering, this figure shows the individual peaks in the periodograms that are used for fitting a Gaussian curve to, as a means to increase the spectral resolution.

then chosen.

As discussed in Section 3.2, there is a variable frequency offset and frequency drift for many reasons. This offset can simply be subtracted by taking the minimum absolute geometric Doppler value for the SPICE simulation and subtracting this from the same point in the real Electra recorded Doppler shift. The variable frequency drift however is far more challenging to overcome. The following processing steps consist of two fitting functions. The first is a form of polynomial fit and the second is a linear bias that ensures that 70-80 km has an electron density profile close to 0 m^{-3} (The reasoning for this assumption is described further on).

4. The frequency drift must be adjusted in order to account for the absence of a USO. An example of this drift can be seen in panel 4 of Figure 5. In order to do this, the tangent point is planned well above the ionosphere for most of the observation duration, so most of the residuum should be at 0 Hz for the majority of the elapsed time. All non-zero values during this vacuum portion of the residuum are known to be artefacts which are most likely due to this frequency drift. This can be removed by fitting a polynomial to the vacuum portion and an additional point in the residuum which corresponds to the time the gradient in the residuum is 0 Hz s⁻¹ (and the tangent point height is about 40 km).. This addition for when the tangent point is within the limb is required as simply extrapolating the polynomial throughout the entire measurement will seldom produce an accurate residuum. This is because the frequency drift during the vacuum portion does not inform what the drift during the limb portion will be as the drift is random and not predictable from the previous portion of the signal. The polynomial fit is not designed to pass through this point exactly, there is an arbitrary frequency offset applied such that the atmospheric portion of the residuum does not cross the 0 Hz axis. This can be seen in Figure 6, where dataset 3F does not cross the 0 Hz axis at the end of the measurement, whereas dataset 2W does, only 3F will produce valid electron density profiles in this case. This frequency offset is set to 0.2 Hz, but this value should be considered of no relevance since the subsequent processing step accounts for all errors introduced by this offset assumption. This value of 0.2 Hz offset is not critical, a further investigation in the appendix shows a parametric test which demonstrates that the following processing step compensates for any assumption made here. Figure 10 in the Appendix goes into more detail of describing this frequency offset resilience. There is one final aspect to this fitting; the polynomial order can vary between 3 and 4 to minimise the error introduced to the regions that are not being fitted over. The introduced error will be larger the further away from the fitted regions, and this error grows if an even higher order polynomial is used. So, the order of the polynomial is kept as low as possible by iterating this fitting process with increasing order until improvements to the χ^2 value over vacuum portion is negligible. Sometimes a 4th-order polynomial is required, but the next measurement will only require a 3rd-order, this order value must be kept dynamic as the frequency drift is inconsistent.
5. One final amendment is required to ensure an accurate residuum. A linear frequency bias is applied to the residuum to guarantee a refractivity close to zero at 70–80 km altitude, whilst not effecting the higher portion of the profile when the tangent point is in the vacuum of space. Typically, for Martian radio occultations, this portion of the profile is always near zero, irrespective of solar activity, SZA variation, and the presence of dust storms (Fox & Yeager, 2006). This is similar to the method carried out by Ao et al., 2015 in their ODY – MRO crosslink occultation demonstration. The subtle difference between the 40 km point and 70-80 km should be reiterated here. The 40 km point is where the gradient in the residuum is 0 Hz s⁻¹, and we use this point to act like an anchor in stage 4 to ensure that the residuum does not pass the 0 Hz x-axis, which would render this stage 5 impossible. The 70-80 km region is the part of the vertical electron density profile where the density is close to zero. This is an iterative process wrapped around an Abel-inversion (Fjeldbo & Eshleman, 1968), which was produced by the International Centre for Theoretical Physics, Trieste, under contract for ESA (Nava et al., 2020). Such that this minimisation algorithm could run as fast as possible, the Abel-inversion MATLAB codebase was converted to python, so that it could be integrated with the existing processing stack. The resultant bias applied is minimal, never rising more than 0.1 mHz s⁻¹.
6. The final residuum from (5) is converted into bending angles and this is then processed through an Abel-inversion to produce a refractivity profile. From this an electron density (N_e) profile is derived by using Equation (2) (Ando et al., 2012)

$$N_e = \frac{n f^2}{\alpha} \quad (2)$$

where

$$\alpha = \frac{e^2}{8\pi^2\epsilon_0 m_e} = -40.2592 \text{ m}^3 \text{ s}^{-2} \quad (3)$$

335 where n is refractivity (dimensionless), f is the transmit frequency of 4.371×10^8 Hz, e is charge of an
336 electron, ϵ_0 is the permittivity of free-space and m_e is the mass of an electron.

5 Results

At the time of writing, 83 mutual ROs have taken place between MEX and TGO. From these, 44 vertical electron density profiles have been extracted. A summary of these profiles can be found in Table 3. There are a multitude of reasons for why this number is far smaller than the total number of occultations. The primary reason is that nine tests occurred with SZA angles greater than 100 degrees (beyond the terminator/on the night side), and with no photoionization at night, only some localized ionization from solar wind electron precipitation (Adams et al., 2018)), and minimal plasma transport. The ionospheric electron densities are below $1 \times 10^{10} \text{ m}^{-3}$ and their effects too weak to currently be extracted from the residuum signal. Therefore, our current processing method is not suitable on the nightside as there are no key residuum features to reference. We will develop an updated technique for extracting the nightside electron densities in the near future, this is a particular challenge due to the absence of a USO

The second category of occultations that could not be analysed are those where MEX was transmitting its HAIL sequence for the first eight tests; this looping 22-second signal was modulated and had regular silence periods. For 75% of the sequences, there was an obtainable carrier wave present. So, these eight datasets still have potential value for proving 'eavesdropping' capability, as will be discussed further in Section 6.

For six of the occultations, the orbits of MEX and TGO were such that the tangent point descended very slowly. The amplitude of the ionospheric features in the residuum is proportional to the derivative of electron density with respect to time. So, if the tangent point descends too slowly then the residuum features can be minimised to a point below the noise floor of $1 \times 10^{10} \text{ m}^{-3}$. Figure 6 has been made to illustrate this point.

Of the 16 remaining measurements, three observations were conducted when the Martian limb was not between the two spacecraft. This was done to test the oscillators' stability in the absence of an atmosphere. Five occultations were unsuccessful due to MEX not transmitting at the correct time. The occurrence of the scheduling errors led to MEX RO transmissions becoming more automated to reduce the probability of future errors. The final eight RO observations where a vertical electron density profile was unobtainable are due to various reasons and require further work to find the root cause.

Figure 8 shows the electron density profiles from two RO measurements, the 49th (named '2I') and the 53rd (named '2M') which occurred on 14/12/22 and 27/12/22 respectively. The profiles do not extend across the full 430 km of altitude because the orbits of MEX and TGO did not allow the tangent point to go to the maximum altitude for all observations. Profile 2M has a maximum altitude of 380 km and 2I is 409 km, this is considered typical as the range of height for a profile we have obtained is 192 - 410 km.

The minimum altitudes for 2M and 2I are 13 km and 27 km respectively. The reason that these datasets do not reach 0 km is twofold. Firstly, the inverse Abel-transform that is used to convert the residuum into a vertical refractivity gradient assumes Mars to be a sphere with a radius equal to the mean Martian radius. This is the same assumption as the models and MARSIS dataset, so they are all readily comparable. The shape of Mars is more closely approximated with a topology modulated ellipsoid. 2M has the coordinates [312.4, -32.6]; since this is in the mid-latitudes, the average Mars radii is a good approximation. In addition, this is in the southern highlands just off the northwest side of Hellas Planitia, so the lowest tangent point for 2M is 0.7 km above the Martian average radius. On the other hand, 2I occurs at [209.2, 65.3], with this high latitude, and the fact that it is in the Panchaia Basin, means that the average Mars radii overestimates by 9 km. Secondly, the SPICE simulations for these two tests showed that they actually occurred 4.84 s and 9.98 s after the instructed time for 2M and 2I respectively. This means that the moment of occultation occurred at a higher altitude than expected. This SPICE simulation delay is significant because this simulation is also the way that the tangent point is calculated, so this delay carries into the altitude readings. This timing error is further worsened by a 5.16 s and 5.02 s delay for 2M and 2I from an unknown cause, which translates to a 6 km vertical uncertainty for both tests.

An explanation for the morphology of these profiles is as follows: the tangent point between the two spacecraft at the beginning of the test is at a high altitude where the Martian ionosphere has a negligible electron density, therefore it has a near-zero effect. As the altitude drops to below 200 km the main ionospheric layer ('M2') is seen with peak electron densities of $1.75 \times 10^{11} \text{ m}^{-3}$ at 141 km and $8.55 \times 10^{10} \text{ m}^{-3}$ at 157 km for 2M and 2I respectively. We find a fainter secondary ionospheric layer (named M1) below the M2 layer, peaking at 110 km for 2M and 145 km for 2I. At deeper altitudes, electron-ion recombination is highly effective, so the electron densities decrease to near zero and the neutral atmosphere becomes dominant. The negative readings on the electron densities axis seen below 50 km correspond to the neutral densities counteracting the effect of the net refractivity from the higher ionospheres. The deep neutral atmosphere will be addressed in a future study.

	RO Number	Dataset Name	Date	UTC Start	UTC of Occultation	Scheme	Longitude (°E)	latitude (°N)	SZA (°)	Max Altitude (km)	Local Solar Time
1	1	I	02/04/21	15:09:00	15:18:16	ingress	144.5	13.1	13.6	399	11:04
2	2	J	06/04/21	03:30:00	03:38:49	ingress	351.9	42.5	33.6	415	11:01
3	3	K	14/04/21	23:32:00	23:33:09	egress	61.1	42.5	82.1	394	05:55
4	4	L	18/05/21	07:07:00	07:08:32	egress	346.1	80.5	62.5	368	11:18
5	5	M	25/05/21	00:08:00	00:09:05	egress	152.5	53.6	36.0	321	11:07
6	7	O	22/07/21	00:06:00	00:07:20	egress	5.5	-7.7	32.2	374	12:18
7	12	T	06/04/22	02:14:21	02:23:47	ingress	224.4	4.0	62.4	387	07:55
8	15	W	27/04/22	13:52:20	13:52:55	egress	13.5	-16.9	71.4	326	15:28
9	17	1A	18/05/22	05:00:27	05:09:23	ingress	276.0	-55.8	39.0	343	10:52
10	18	1B	27/05/22	13:21:22	13:22:00	egress	245.6	17.6	40.9	407	10:59
11	19	1C	01/06/22	11:01:00	11:09:50	ingress	263.4	-35.2	68.7	347	06:46
12	21	1E	13/06/22	03:18:23	03:28:08	ingress	288.2	-13.6	72.9	350	17:07
13	22	1G	30/06/22	14:06:29	14:15:16	ingress	260.8	-47.2	39.1	379	14:41
14	23	1H	08/07/22	10:46:11	10:55:28	ingress	16.9	-47.2	32.2	379	13:57
15	25	1J	19/07/22	19:49:30	19:58:45	ingress	322.2	-30.3	5.2	380	11:56
16	32	1Q	25/08/22	09:02:31	09:03:14	egress	164.1	21.2	62.2	397	14:37
17	33	1R	30/08/22	14:49:09	14:49:57	egress	111.7	23.2	58.7	391	13:30
18	36	1U	17/09/22	04:50:41	04:51:41	egress	346.0	-59.3	50.8	371	07:44
19	37	1V	19/09/22	06:00:57	06:01:21	egress	349.8	-54.5	59.4	379	07:49
20	39	1X	13/10/22	15:14:55	15:14:54	egress	227.3	-50.8	58.0	334	17:08
21	41	1Z	27/10/22	20:43:17	20:52:23	ingress	240.2	46.6	65.9	425	14:28
22	42	2A	31/10/22	09:34:47	09:35:14	egress	46.1	-33.0	69.8	367	11:58
23	43	2B	11/11/22	04:36:05	04:36:43	egress	167.7	29.4	68.0	399	08:11
24	45	2E	27/11/22	07:47:32	07:56:41	ingress	289.0	-82.2	67.4	379	11:12
25	48	2H	07/12/22	14:38:51	14:39:33	egress	45.0	23.9	80.2	403	17:09
26	49	2I	14/12/22	06:03:10	06:04:38	egress	209.2	65.3	76.6	409	15:17
27	50	2J	19/12/22	19:33:50	19:34:17	egress	44.6	42.0	53.1	418	14:15
28	51	2K	21/12/22	22:19:24	22:28:18	ingress	3.7	-39.7	41.4	380	13:05
29	52	2L	22/12/22	16:28:43	16:29:09	egress	96.8	58.7	60.3	377	12:49
30	53	2M	27/12/22	04:07:52	04:16:36	ingress	312.4	-32.6	32.8	380	12:07
31	54	2N	03/01/23	08:44:08	08:53:03	ingress	294.4	-7.9	27.0	353	10:18
32	57	2Q	27/01/23	01:14:13	01:23:28	ingress	214.2	11.7	73.5	384	07:02
33	58	2R	01/02/23	03:27:34	03:37:18	ingress	227.0	83.5	81.0	397	06:52
34	59	2S	09/02/23	00:07:25	00:16:29	ingress	4.8	76.8	75.5	407	07:42
35	60	2T	15/02/23	17:21:54	17:31:12	ingress	230.6	72.9	62.7	391	11:44
36	61	2U	23/02/23	14:03:27	14:12:27	ingress	339.4	64.1	31.8	368	10:40
37	62	2V	26/02/23	18:39:46	18:48:46	ingress	275.1	61.8	83.5	365	08:58
38	63	2W	10/03/23	03:53:34	04:02:40	ingress	298.7	45.2	77.4	359	12:31
39	67	3A	05/04/23	09:16:49	09:17:24	egress	49.6	-51.8	40.2	380	08:28
40	69	3C	17/04/23	14:21:09	14:22:09	egress	151.3	-57.5	25.8	381	12:33
41	70	3D	25/04/23	03:53:28	04:02:18	ingress	51.4	40.9	28.9	417	14:44
42	71	3E	02/05/23	20:57:44	21:06:43	ingress	205.9	28.0	48.9	410	13:50
43	72	3F	08/05/23	06:20:01	06:29:18	ingress	123.3	42.5	13.5	416	13:37
44	73	3G	15/05/23	05:34:23	05:43:25	ingress	230.2	62.3	87.5	429	15:32

Table 3: A summary of the 44 RO observations for which electron density profiles have been calculated.

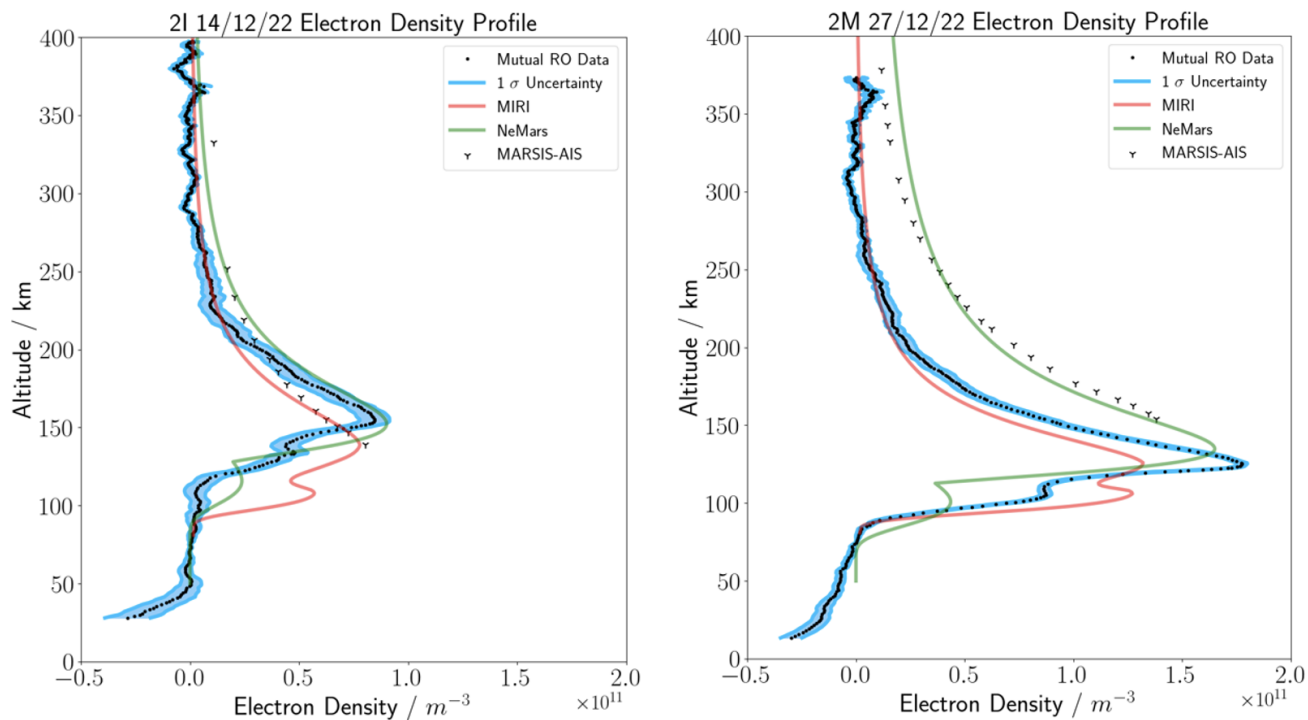


Figure 8: Electron density profiles for two mutual RO observations. 2I (left panel) is from an egress configuration with a high SZA value of 77° and 2M (right panel) is from an ingress with a SZA close to noon with 33° . 0 km on the y-axis indicates the average mars radii of 3389.1, not the ground. The blue envelope is the result of a numerical error-propagation with 100 iteration. There is a vertical uncertainty of 6 km for both profiles. Also included are comparisons with NeMars (Sánchez-Cano et al., 2013) ([sanchez-cano solar 2016](#)) and Mars Initial Reference Ionosphere Model (MIRI) (Mendillo et al., 2013) semi-empirical models. The model inputs for 27/12/22 are SZA 32° , Coordinates [312,-32], $F_{10.7}$ 151.7, Mars Solar Distance 1.558 AU. The inputs for 14/12/22 are SZA 76° , Coordinates [209,65], $F_{10.7}$ 157.4, Mars Solar Distance 1.541 AU. Data from MARSIS-AIS is also superimposed, effort was made to find measurements with similar SZA. The specific MARSIS dataset for 2I is OrbitNumber:10424, IonosondeNumber:225 and the for 2M; OrbitNumber:10675, IonosondeNumber:93.

396 The two profiles differ from each other principally because of the different values for SZA. 2M occurs closer to
 397 noon with a SZA value of 32.8° and 2I is nearer the terminator with 76.7° . These profiles follow the behaviour
 398 expected from an ionosphere dominated by photoionization. The reduced photoionization and higher SZA at 2I
 399 causes the M2 peak density to decrease and the peak altitude to be higher (Fox & Yeager, 2006).

400
 401 For further validation, we are in the following comparing our profiles to other observations and to two ionosphere
 402 models. The Y-crosses in Figure 8 are electron density profiles from the Mars Advanced Radar for Subsurface and
 403 Ionosphere Sounding (MARSIS) onboard the Mars Express spacecraft in its Active Ionospheric Sounding (AIS)
 404 mode (Gurnett et al., 2008), and have been retrieved via the methodology described in Sánchez-Cano et al., 2012.
 405 This instrument uses a chirp signal to sound the top side of the ionosphere. Similar to a discussion point in Section
 406 6, a signal is reflected from an ionospheric volume when its plasma frequency is higher than the signal's frequency.
 407 In order to determine the plasma frequency, MARSIS sequentially increases the transmit frequency until reflection
 408 ceases (Jordan et al., 2009). The altitude where this happens is determined by monitoring the time for the last
 409 echo to be received. These plasma frequencies and altitudes can be combined to make topside electron density
 410 profiles. The altitudes below the M2 peak cannot be probed with this method.

411
 412 Two models have been superimposed in Figure 8. The NeMars (Sánchez-Cano et al., 2013) model is shown in
 413 green. This is an empirical model based of data from MEX's Mars Advanced Radar and Ionospheric Sounding
 414 experiment (MARSIS) and Mars Global Surveyor (MGS) conventional RO. The other model in red is the Mars
 415 Initial Reference Ionosphere (MIRI) Model (Mendillo et al., 2013). This model is similar to NeMars where it uses
 416 a mostly MARSIS data and smaller amount of MGS conventional RO data, but also includes MEX MaRS conven-
 417 tional RO data too (Pätzold et al., 2004). In addition, this is a semiempirical model, meaning that its numerical
 418 parameterisations are guided by underlying known physical ionospheric behaviour. At 2I, our observations show
 419 good consistency with NeMars but the MIRI profiles have a lower M2 peak altitude and a more developed M1
 420 layer. This result is similar to the findings in Ao et al., 2015, where they also compared with NeMars. At 2M, our

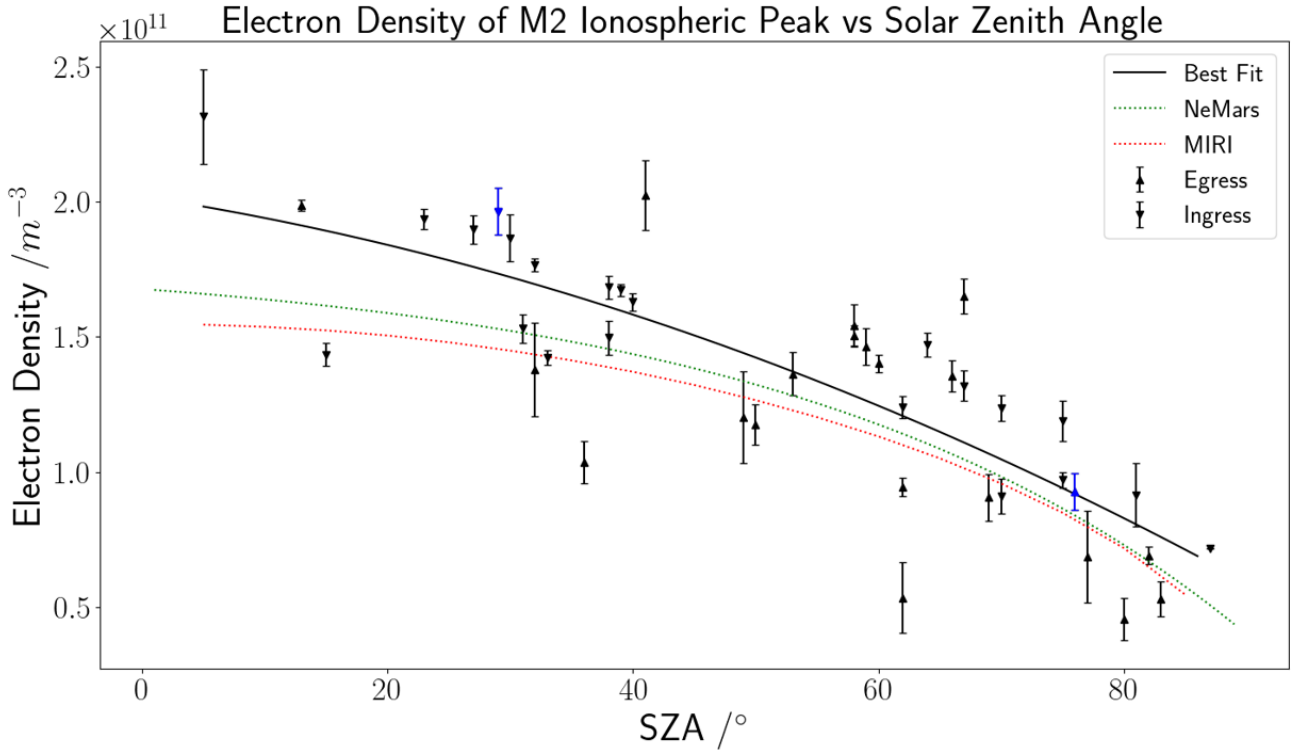


Figure 9: The trend of M2 ionospheric peak electron densities reducing with increasing Solar Zenith Angles (SZA). The black solid line is the least-mean-square quadratic fit ($-1 \times 10^7 x^2 - 7 \times 10^8 x + 2 \times 10^{11}$) of all occultations with correlation R value of 0.807. Comparisons can be seen for the NeMars (Sánchez-Cano et al., 2013) and Mars Initial Reference Ionosphere Model (MIRI) (Mendillo et al., 2013) models. The two blue markers indicate the measurements that are shown in Figure 8. The inputs to these models are for conditions which match dataset 2M (shown in Table 3). Specifically these inputs are Coordinates [2,-32], $F_{10.7}$ is 151.7, and the Mars Solar Distance is 1.558 AU.

421 topside ionosphere and M2 peak altitude are consistent with MIRI, but our M2 peak density is larger than MIRI's
 422 by around 50%. The NeMars topside ionospheric densities are about a factor of 2 larger than ours but the M2 peak
 423 altitude and density are more consistent. A forthcoming study will investigate these differences in more detail.

424
 425 For a broader validation of our observations, we are also looking at the trend with SZA of the M2 peak densities,
 426 as showing in Figure 9. Super-imposed in the figure alongside our observations are again values from NeMars
 427 (green) and MIRI (red). As seen by the best fit curve to our occultation data (black line), there is a clear trend of
 428 peak ionospheric densities decreasing for increasing zenith angles, consistent with the expectations for an iono-
 429 sphere dominated by solar photoionization. Our observed M2 peak values and SZA trend are consistent with those
 430 of both NeMars and MIRI, with the minor differences probably being due to factors not considered by the models.

431
 432 Also visible in Figures 8 and 9 are error bars (in Figures 8 illustrated as blue envelopes). These have been calcu-
 433 lated following the methodology of Müller-Wodarg et al., 2006 via a numerical error propagation of 100 iterations
 434 with a 5% input error. Specifically, this error calculation was carried out by adding this 5% input error to the car-
 435 rier signal frequency extracted during step one of Figure 5, then noting the change in the final vertical profile. As
 436 stated in Section 3.3, the frequency error of 3.6 mHz was far lower than the noise observed in the residuums. 5%
 437 was calculated from the ratio of the magnitude of a typical M2 ionospheric residuum feature to the short-timescale
 438 noise. The source of this noise will be determined once full oscillator characterisation has taken place.

440 6 Discussion and Recommendations

441 We have shown that mutual radio occultation is a powerful method for sampling the ionospheres of planets.
 442 Despite the limitations encountered in our experiments, most notably the absence of a USO, we have through
 443 very careful analysis of the returned Doppler shifts been able to extract multiple ionospheric profiles which show
 444 ionospheric behaviour consistent with expectations. One of the most powerful advantages of our method has been

the ability to sample all dayside solar zenith angles and thereby for the first time obtain a remote sensing method for sampling the Martian ionosphere in full 3-D.

Our feasibility study has also revealed how the method can be further improved upon in a number of ways. As stated in subsection 3.2, the lack of the USO onboard TGO caused a variable frequency offset (varying from -610 to -680 Hz). This has been improved by changing an internal time conversion constant within Electra's firmware via a telemetry update; now the offset ranges from 97 to 149 Hz. Additionally, this oscillator instability led to a minimisation being required to ensure that 80 km is close to zero refractivity, this further worsened the uncertainty in electron density profiles as other vertical features could be inadvertently altered to ensure this 80 km zero point. Electra can record a time precision of 15 ns, which is ample precision for this mutual radio occultation purpose. However, in the absence of a USO, it is recommended that the timestamps from the local oscillator be calibrated against a more accurate USO timestamps onboard the spacecraft at regular intervals throughout the test. This can be achieved by incorporating the spacecraft's extended telemetry. This would also improve the variable Electra timestamp accuracy, which made simulating the geometric Doppler difficult, as stated in Section 4. This has been done for the most recent RO observations, where the difference between the commanding and actual start time has been reduced from ± 16 seconds to around $+4$ seconds.

There are several discoveries and improvements that should be noted. Figure 7 shows multiple spectral features in the spectrogram, where three arcs can be seen to converge throughout the RO observation. These are either side of the main carrier tone and are visibly fainter. This is a result of multipath reflections from the surface. At any time during observation, the two lines are equally spaced from the main carrier tone (which is determined by being the highest spectral density), and as the tangent point descends to the surface, these three lines converge as the occultation begins and the radio link is interrupted by the surface of Mars. As the tangent point falls, the path differential between the line-of-sight and reflected signal path becomes smaller. The fainter third peak is a mirror frequency as a result of the downconverted step in Electra. The periodograms show that the spectral peaks become finer closer to the time of occultation. This is likely due to the fact that the shallower the path gets over the surface the less scattering points there are contributing to the scattering.

Although this has not been done for the events described in this report, mutual RO has the potential to 'eavesdrop' on other passing radio communications. Despite terrestrial global navigation satellite system (GNSS) satellites not transmitting signals that are specifically designed to be used by RO satellites; such as COSMIC (Ho et al., 2020), CHAMP and other RO satellites use them regardless. For example, there is the potential to use Mars Relay System communication links to probe the Martian ionosphere and atmosphere, provided that the carrier frequency is obtainable. If telemetry can successfully be filtered out of the sidebands, then minutia in the carrier frequency can be ascertained. Practically, this transpires as MEX and TGO not needing dedicated pointing, power, and total downlink resources, as it would be dual-purpose with other SC-SC or SC-lander communications. This would increase the number of opportunities available to conduct mutual RO. This would be a similar operation to Ao et al., 2015, where the signal used for RO was a modulated transmission intended for either the Spirit or Opportunity rovers. In theory, any signal should be usable, so long as a stable carrier tone can be isolated.

In addition to eavesdropping, this method could be improved from an operational standpoint by doing RO simultaneously in two or more frequencies. As explained in Section 3.3, mutual RO is especially effective for measuring ionospheres at these UHF frequencies. From this study, we have found a maximum electron density of $2.4 \times 10^5 \text{ cm}^{-3}$ leading to a plasma frequency of 4.4 MHz. At this 437.1 MHz frequency, a propagating radio wave will be greatly affected by the refractive properties of the cold ionospheric plasma, leading to UHF observations being specifically sensitive to the Martian ionosphere. A second frequency in dual-band could be selected such that the ionospheric and neutral atmospheric contributions to net refractivity along the radio link could be separated. This could be achieved by transmitting two tones that are far enough apart in the spectrum. For example, ample separation could be achieved with a UHF and an X-band link (around 0.44 and 8GHz). This is similar to MEX's MaRS instruments which uses dual frequency phase coherent downlinks in S and X band. (Pätzold et al., 2004). This recommendation should only be considered for future missions as both MELACOM and Electra lack this capability.

7 Conclusions

There has been a resurgence of interest in mutual radio occultation in recent years. Now that ESA has two spacecraft orbiting another planet, this technique can be investigated and the instrumentation refined. Typically, radio occultation observations for other planets have the receiver on the Earth's surface, but this constrains the breadth of locations and SZA that can be measured. It also introduces errors as the signal must pass through dispersive space between the two planets and through the Earth's relatively dense ionosphere and moist atmosphere. Mutual

502 RO alleviates these problems by placing both the receiver and transmitter in orbit around the same planet. The
 503 hardware for these observations has been detailed. The constant carrier is being sent from MEX's MELACOM
 504 antenna to TGO's Electra antenna through the Martian limb. None of this equipment was designed for this appli-
 505 cation, so several techniques have been applied to obtain acceptable results. The firmware on both satellites was
 506 updated, and the advantageous orbital parameters were determined. A new processing chain was developed to
 507 overcome the hardware's limitations. The most significant of these constraints is the lack of a USO, which led to
 508 a retrieval process including a minimisation step that ensured that the refractivity at 70-80 km altitude was near
 509 zero.

510 Mutual RO has the potential to allow a vast (several order of magnitude) increase in radio occultation oppor-
 511 tunities, compared to spacecraft-to-earth RO. However, the true value of mutual RO will only be realised once
 512 simultaneous RO observations can occur across multiple satellites, similar to terrestrial occultation constellations.
 513 This will leverage the existing equipment already placed in orbit around Mars or other planets by ESA and its
 514 partners. 'Eavesdropping' will be essential for this to happen, such that mutual RO can be dual-purpose with relay
 515 activities.
 516

517 This article has demonstrated the success of this feasibility study and highlighted essential engineering consider-
 518 ations to improve when designing for future missions. These tests are ongoing; at the time of writing, there is
 519 roughly one mutual RO observation per week for the foreseeable future. While the physical hardware cannot be
 520 altered, this process will be further improved once the aged Electra oscillator is better characterised. Ultimately,
 521 this article has shown an economic way to garner extra scientific returns from non-specialised equipment and
 522 should encourage future missions to include mutual RO as a viable capability.
 523

524 8 Acknowledgements

525 J.P acknowledges his UK Science and Technology Facilities Council (STFC) Ph.D. Bursary ST/T506151/1 and the
 526 ongoing support of the ESA Science Operations Centre and Mission Operations Centre teams.

527 IMW is grateful for the support from UK-STFC grant ST/S000364/1.

528 B.S.-C. acknowledges support through UK-STFC Ernest Rutherford Fellowship ST/V004115/1.

529 A.C.-M. acknowledges IAA-CSIC team is supported by grant PID2022-137579NB-I00 funded by
 530 MCIN/AEI/10.13039/501100011033 and by "ERDF A way of making Europe".

531 B.N. and Y.M.-O. acknowledge ESA support through Contract No. 4000127090/19/NL/IB/gg.

532 The authors thank Harvey Elliot and Austin Lazaro at JPL for their assistance in constraining the Electra time-
 533 stamps.

534 Data Availability

535 Figure 9 data points are at <https://doi.org/10.6084/m9.figshare.24125850.v1> (Parrott, 2023b)

536

537 Table 3 at <https://doi.org/10.6084/m9.figshare.24125958.v1> (Parrott, 2023c)

538

539 Associated data products from datasets 2I (14/12/22) and 2M (27/12/22):

540 -Vertical Electron Density Profiles, <https://doi.org/10.6084/m9.figshare.24125895.v1> (Parrott, 2023a)

541 -Total Doppler Shift, <https://doi.org/10.6084/m9.figshare.25138349.v1> (Parrott, 2024b)

542 -In-phase and quadrature data,

543 <https://doi.org/10.6084/m9.figshare.25138334.v1> (Parrott, 2024a)

544 References

545 Acton, C., Bachman, N., Semenov, B., & Wright, E. (2018). A Look Towards the Future in the Handling of Space
 546 Science Mission Geometry. *Planetary and Space Science*, 150, 9–12. [https://doi.org/10.1016/j.pss.2017.
 547 02.013](https://doi.org/10.1016/j.pss.2017.02.013)

548 Acton, C. H. (1996). Ancillary data services of NASA's Navigation and Ancillary Information Facility. *Planetary and
 549 Space Science*, 44(1), 65–70. [https://doi.org/10.1016/0032-0633\(95\)00107-7](https://doi.org/10.1016/0032-0633(95)00107-7)

550 Adams, D., Xu, S., Mitchell, D. L., Lillis, R. J., Fillingim, M., Andersson, L., Fowler, C., Connerney, J. E. P., Espley,
 551 J., & Mazelle, C. (2018). Using Magnetic Topology to Probe the Sources of Mars' Nightside Ionosphere.
 552 *Geophysical Research Letters*, 45(22), 12, 190–12, 197. <https://doi.org/10.1029/2018GL080629>

- 553 Ando, H., Imamura, T., Nabatov, A., Futaana, Y., Iwata, T., Hanada, H., Matsumoto, K., Mochizuki, N., Kono, Y.,
554 Noda, H., Liu, Q., Oyama, K.-I., Yamamoto, Z., & Saito, A. (2012). Dual-Spacecraft Radio Occultation Mea-
555 surement Of The Electron Density Near The Lunar Surface By The SELENE Mission. *Journal of Geophysical*
556 *Research: Space Physics*, 117(A8). <https://doi.org/10.1029/2011JA017141>
- 557 Ao, C. O., Edwards, C. D., Kahan, D. S., Pi, X., Asmar, S. W., & Mannucci, A. J. (2015). A first demonstration of
558 Mars crosslink occultation measurements. *Radio Science*, 50(10), 997–1007. [https://doi.org/10.1002/](https://doi.org/10.1002/2015RS005750)
559 [2015RS005750](https://doi.org/10.1002/2015RS005750)
- 560 Ball, A. J., Blancquaert, T., Bayle, O., Lorenzoni, L. V., Haldemann, A. F. C., & the Schiaparelli EDM team. (2022).
561 The ExoMars Schiaparelli Entry, Descent and Landing Demonstrator Module (EDM) System Design. *Space*
562 *Science Reviews*, 218(5), 44. <https://doi.org/10.1007/s11214-022-00898-z>
- 563 Born, M., & Wolf, E. (2019). *Principles of optics* (Seventh anniversary edition, 60th anniversary of first edition,
564 20th anniversary of seventh edition). Cambridge University Press.
- 565 Bridges, J. C., Clemmet, J., Croon, M., Sims, M. R., Pullan, D., Muller, J.-P., Tao, Y., Xiong, S., Putri, A. R., Parker,
566 T., Turner, S. M. R., & Pillinger, J. M. (2017). Identification of the Beagle 2 lander on Mars. *Royal Society*
567 *Open Science*, 4(10), 170785. <https://doi.org/10.1098/rsos.170785>
- 568 Cardesin-Moinelo, A., Godfrey, J., Grotheer, E., Blake, R., Damiani, S., Wood, S., Dressler, T., Bruno, M., Johnstone,
569 A., Lucas, L., Marin-Yaseli de la Parra, J., Merritt, D., Sierra, M., Määttänen, A., Antoja-Lleonart, G., Breit-
570 fellner, M., Muniz, C., Nespoli, F., Riu, L., . . . Wilson, C. (2024). Mars Express: 20 Years of Mission, Science
571 Operations and Data Archiving. *Space Science Reviews*, 220(2), 25. [https://doi.org/10.1007/s11214-024-](https://doi.org/10.1007/s11214-024-01059-0)
572 [01059-0](https://doi.org/10.1007/s11214-024-01059-0)
- 573 Cardesin-Moinelo, A., Geiger, B., Lacombe, G., Ristic, B., Costa, M., Titov, D., Svedhem, H., Marín-Yaseli, J., Merritt,
574 D., Martin, P., López-Valverde, M., Wolkenberg, P., & Gondet, B. (2021). First year of coordinated science
575 observations by Mars Express and ExoMars 2016 Trace Gas Orbiter. *Icarus*, 353, 113707. [https://doi.org/](https://doi.org/10.1016/j.icarus.2020.113707)
576 [10.1016/j.icarus.2020.113707](https://doi.org/10.1016/j.icarus.2020.113707)
- 577 C-MAC. (2005). Crystal Product Data Book 2000. Retrieved August 1, 2023, from [http://lars.mec.ua.pt/public/](http://lars.mec.ua.pt/public/LAR%20Projects/Laser3D/2003_MiguelMatos/Componentes/crystal%20oscillators%20catalogue.pdf)
578 [LAR%20Projects/Laser3D/2003_MiguelMatos/Componentes/crystal%20oscillators%20catalogue.pdf](http://lars.mec.ua.pt/public/LAR%20Projects/Laser3D/2003_MiguelMatos/Componentes/crystal%20oscillators%20catalogue.pdf)
- 579 Edwards, C. D. (2003). The Electra Proximity Link Payload for Mars Relay Telecommunications and Navigation.
580 *54th International Astronautical Congress of the International Astronautical Federation, the International*
581 *Academy of Astronautics, and the International Institute of Space Law*. [https://doi.org/10.2514/6.IAC-03-](https://doi.org/10.2514/6.IAC-03-Q.3.a.06)
582 [Q.3.a.06](https://doi.org/10.2514/6.IAC-03-Q.3.a.06)
- 583 European Space Agency & ESA SPICE Service. (2019a). ExoMars 2016 SPICE Kernel Dataset [Institution: European
584 Space Agency]. <https://doi.org/10.5270/esa-pwviqkg>
- 585 European Space Agency & ESA SPICE Service. (2019b). Mars Express SPICE Kernel Dataset [Institution: European
586 Space Agency]. <https://doi.org/10.5270/esa-trn5vp1>
- 587 Fjeldbo, G., & Eshleman, V. R. (1968). The atmosphere of mars analyzed by integral inversion of the Mariner
588 IV occultation data. *Planetary and Space Science*, 16(8), 1035–1059. [https://doi.org/10.1016/0032-](https://doi.org/10.1016/0032-0633(68)90020-2)
589 [0633\(68\)90020-2](https://doi.org/10.1016/0032-0633(68)90020-2)
- 590 Fox, J. L., & Yeager, K. E. (2006). Morphology of the near-terminator Martian ionosphere: A comparison of models
591 and data. *Journal of Geophysical Research*, 111(A10), A10309. <https://doi.org/10.1029/2006JA011697>
- 592 Gurnett, D., Huff, R., Morgan, D., Persoon, A., Averkamp, T., Kirchner, D., Duru, F., Akalin, F., Kopf, A., Nielsen, E.,
593 Safaeinili, A., Plaut, J., & Picardi, G. (2008). An overview of radar soundings of the martian ionosphere
594 from the Mars Express spacecraft. *Advances in Space Research*, 41(9), 1335–1346. [https://doi.org/10.](https://doi.org/10.1016/j.asr.2007.01.062)
595 [1016/j.asr.2007.01.062](https://doi.org/10.1016/j.asr.2007.01.062)
- 596 Gurvits, L. I. (2014, January). *Observation and Detection of Mars Express UHF Radio Signal with the Arecibo Telescope*
597 (tech. rep. No. 13-017). Joint Institute for VLBI in Europe. Dwingeloo, The Netherlands.
- 598 Ho, S., Anthes, R. A., Ao, C. O., Healy, S., Horanyi, A., Hunt, D., Mannucci, A. J., Pedatella, N., Randel, W. J.,
599 Simmons, A., Steiner, A., Xie, F., Yue, X., & Zeng, Z. (2020). The COSMIC/FORMOSAT-3 Radio Occultation
600 Mission after 12 Years: Accomplishments, Remaining Challenges, and Potential Impacts of COSMIC-2.
601 *Bulletin of the American Meteorological Society*, 101(7), E1107–E1136. [https://doi.org/10.1175/BAMS-D-](https://doi.org/10.1175/BAMS-D-18-0290.1)
602 [18-0290.1](https://doi.org/10.1175/BAMS-D-18-0290.1)
- 603 Jordan, R., Picardi, G., Plaut, J., Wheeler, K., Kirchner, D., Safaeinili, A., Johnson, W., Seu, R., Calabrese, D.,
604 Zampolini, E., Cicchetti, A., Huff, R., Gurnett, D., Ivanov, A., Kofman, W., Orosei, R., Thompson, T.,
605 Edenhofer, P., & Bombaci, O. (2009). The Mars express MARSIS sounder instrument. *Planetary and Space*
606 *Science*, 57(14-15), 1975–1986. <https://doi.org/10.1016/j.pss.2009.09.016>
- 607 Mendillo, M., Marusiak, A. G., Withers, P., Morgan, D., & Gurnett, D. (2013). A new semiempirical model of
608 the peak electron density of the Martian ionosphere. *Geophysical Research Letters*, 40(20), 5361–5365.
609 <https://doi.org/10.1002/2013GL057631>
- 610 Müller-Wodarg, I. C. F., Yelle, R. V., Borggren, N., & Waite, J. H. (2006). Waves and horizontal structures in
611 Titan’s thermosphere. *Journal of Geophysical Research*, 111(A12), A12315. [https://doi.org/10.1029/](https://doi.org/10.1029/2006JA011961)
612 [2006JA011961](https://doi.org/10.1029/2006JA011961)

- 613 Nava, B., Kashcheyev, A., Migoya-Orue, Y., Radicella, S. M., Parrott, J., Sánchez-Cano, B., Witasse, O., Svedhem,
614 H., Titov, D., & Ao, C. O. (2020, October). *Mutual radio occultation experiment between ExoMars Trace Gas*
615 *Orbiter and Mars Express: Feasibility study and preparation for the data analysis* (tech. rep.). Abdus Salam
616 Centre of International Physics. Trieste. <https://doi.org/10.5194/epsc2020-299>
- 617 Parrott, J. (2023a). Electron Density Profiles [Dataset]. <https://doi.org/10.6084/M9.FIGSHARE.24125895.V1>
- 618 Parrott, J. (2023b). M2 Electron Density and SZA [Dataset]. [https://doi.org/10.6084/M9.FIGSHARE.24125850.](https://doi.org/10.6084/M9.FIGSHARE.24125850.V1)
619 V1
- 620 Parrott, J. (2023c). Mutual Occultation Specification Table [Dataset]. [https://doi.org/10.6084/M9.FIGSHARE.](https://doi.org/10.6084/M9.FIGSHARE.24125958.V1)
621 24125958.V1
- 622 Parrott, J. (2024a). Compressed Inphase and Quadrature data [Dataset]. [https://doi.org/10.6084/M9.FIGSHARE.](https://doi.org/10.6084/M9.FIGSHARE.25138334.V1)
623 25138334.V1
- 624 Parrott, J. (2024b). Net Doppler (Residuum + Geometric Doppler) [Dataset]. [https://doi.org/10.6084/M9.](https://doi.org/10.6084/M9.FIGSHARE.25138349.V1)
625 FIGSHARE.25138349.V1
- 626 Pätzold, M., Neubauer, F. M., Carone, L., Hagermann, A., Stanzel, C., Häusler, B., Remus, S., Selle, J., Hagl, D.,
627 Hinson, D. P., Simpson, R. A., Tyler, G. L., Asmar, S. W., Axford, W. I., Hagfors, T., Barriot, J. .-, Cerisier,
628 J. .-, Imamura, T., Oyama, K. .-, ... Dehant, V. (2004). MaRS: Mars Express Orbiter Radio Science
629 [Conference Name: Mars Express: the Scientific Payload ADS Bibcode: 2004ESASP1240..141P], 1240,
630 141–163. Retrieved July 14, 2023, from <https://ui.adsabs.harvard.edu/abs/2004ESASP1240..141P>
- 631 Sánchez-Cano, B., Radicella, S., Herraiz, M., Witasse, O., & Rodríguez-Caderot, G. (2013). NeMars: An empirical
632 model of the martian dayside ionosphere based on Mars Express MARSIS data. *Icarus*, 225(1), 236–247.
633 <https://doi.org/10.1016/j.icarus.2013.03.021>
- 634 Sánchez-Cano, B., Witasse, O., Herraiz, M., Radicella, S. M., Bauer, J., Blelly, P.-L., & Rodríguez-Caderot, G. (2012).
635 Retrieval of ionospheric profiles from the Mars Express MARSIS experiment data and comparison with
636 radio occultation data. *Geoscientific Instrumentation, Methods and Data Systems*, 1(1), 77–84. [https://doi.](https://doi.org/10.5194/gi-1-77-2012)
637 [org/10.5194/gi-1-77-2012](https://doi.org/10.5194/gi-1-77-2012)
- 638 Tamburo, P., Withers, P., Dalba, P. A., Moore, L., & Koskinen, T. (2023). Cassini Radio Occultation Observations of
639 Saturn’s Ionosphere: Electron Density Profiles From 2005 to 2013. *Journal of Geophysical Research: Space*
640 *Physics*, 128(4), e2023JA031310. <https://doi.org/10.1029/2023JA031310>
- 641 Taylor, J., Lee, D., & Shambayati, S. (2006, September). *Mars Reconnaissance Orbiter Telecommunications* (tech.
642 rep.). Jet Propulsion Laboratory. Pasadena, California.
- 643 Withers, P., Felici, M., Mendillo, M., Moore, L., Narvaez, C., Vogt, M. F., Oudrhiri, K., Kahan, D., & Jakosky, B. M.
644 (2020). The MAVEN Radio Occultation Science Experiment (ROSE). *Space Science Reviews*, 216(4), 61.
645 <https://doi.org/10.1007/s11214-020-00687-6>

646 9 Appendix

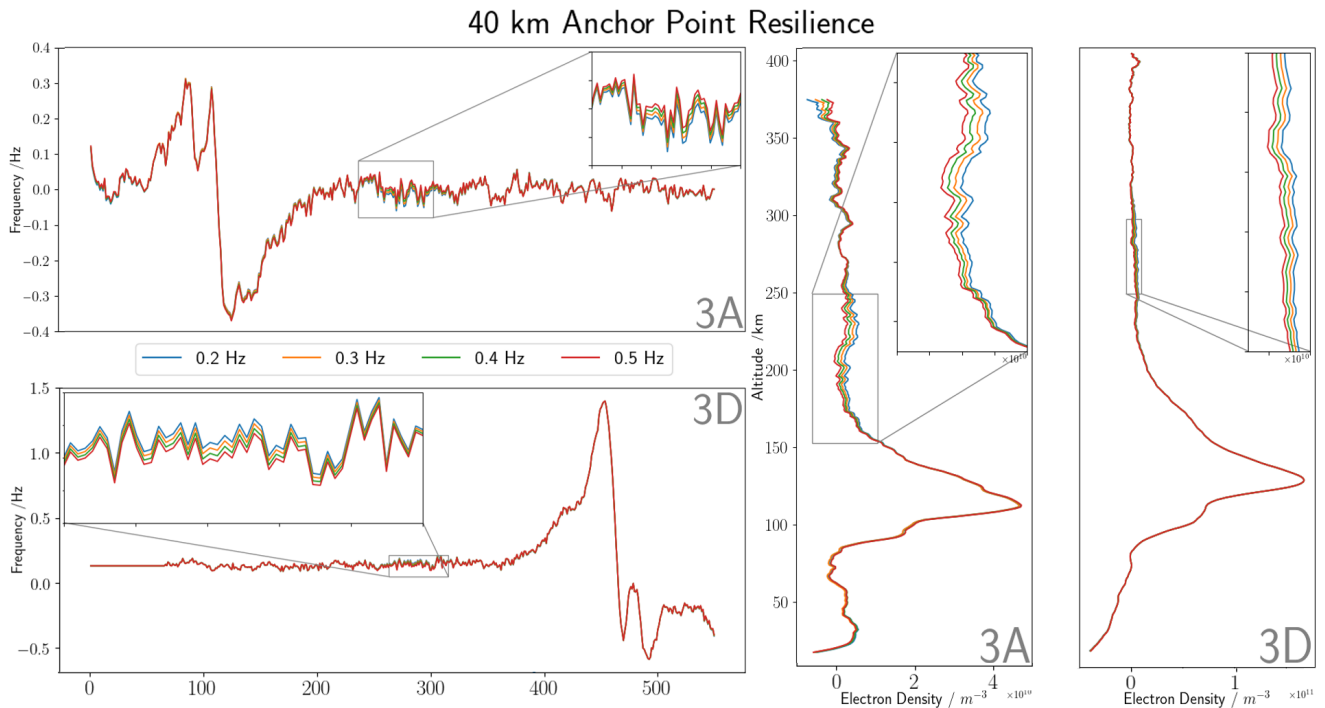


Figure 10: Two examples of a residuum and profile that show how the arbitrary frequency offset on the 40 km point has a near-negligible effect. Dataset 3A is an egress mutual radio occultation and the 40 km anchor point would be at around 30 seconds, whereas on the ingress dataset 3D, the anchor point would be at 550 seconds. Four different amounts of frequency offset are shown, starting from 0.2 Hz and finishing with 0.5 Hz

647 Although the vertical offset used during the first fitting in the processing is selected arbitrarily, the final results
 648 are very resilient to any error that may be introduced with this assumption. For convenience, the method for
 649 the application of the arbitrary offset shall be repeated from step four of section 4. This vertical offset marks
 650 the distance from the 0 Hz axis that the polynomial fit must pass through to ensure that the residuum does not
 651 cross the 0 Hz axis. For the results shown in this article, a 40 km point vertical offset was set to 0.2 Hz, but this
 652 value matters little, as the second fitting corrects for this. If the first fitting results in a residuum with a non-
 653 physical form, it is accounted for later in the processing chain since the second fitting brings the 70-80 km
 654 region in the electron density profiles close to 0 m^{-3} . Figure 10 supports this, by showing the variation in residuum and
 655 resultant electron density profiles vary very little, even when a vertical offset of 0.5 Hz is applied to the 40 km
 656 point. Also, this variation is only seen around 300 s on each residuum because this is the middle of measurement.
 657 Step four does not have any effect on the high altitude portion of the residuum, and step five then corrects for any
 658 changes that have occurred at the low altitude portions. Thus, leaving just the middle of the residuum to display
 659 any variance.